Electronic Supplementary Information

Tree-inspired braiding fibrous framework enabling high-efficiency and salt-rejecting solar evaporation

Duo Xu, ‡[ab] Can Ge, ‡[b] Ze Chen, ‡[a] Yingcun Liu, [b] Tao Chen, [a] Chong Gao, [a] Keshuai Liu, [a] Weilin Xu, [a] Qian Zhang, *[a] Jian Fang*[b]

Author Contributions:‡Duo Xu, Can Ge, and Ze Chen contributed equally to this work.

[a] State Key Laboratory of New Textile Materials and Advanced Processing Technologies, Wuhan Textile University, Wuhan 430200, China.

[b] College of Textile and Clothing Engineering, Soochow University, Suzhou 215123, China.

E-mail: qzhang@wtu.edu.cn (Q.Z.)

jian.fang@suda.edu.cn (J.F.)

This PDF file includes:

Experiment section

Fig. S1 to S25, Table S1.

EXPERIMENTAL SECTION

Materials: Carbon fiber bundles (T300-1K), and Tencel yarns (19.7 tex), are purchased from Toray Co. LTD and Anhui Huamao Co. LTD, respectively. Pyrrole and ferric trichloride are purchased from Sinopharm Group Chemical Reagent Co. Ltd., China. Anhydrous ethanol is purchased from Aladdin.

Fabrication of BCFF: The carbon fibers and Tencel are first sonicated in anhydrous ethanol at 60 ℃ for 1 h to remove impurities. The well-wound Tencels are immersed in a 0.12 mol/L pyrrole monomer solution for 0.5 h, then extracted and placed in a 0.18 mol/L solution of ferric chloride for 2 h, during which the solution is stirred. Finally, the PPy coating layer is applied onto the Tencels via polymerization. Carbon/Tencel braided yarns (CTBY) are fabricated via braiding using a high-speed rope braiding machine. The carbon fiber bundles are sequentially wound onto the bobbin and secured to the yarn disc on the outside. In addition, the core PPy@Tencels are wound on a constant bobbin and fed via a pre-tension device. The core-shell CTBY produced by the carbon fiber bundles is helically interlocked onto the PPy@Tencels as the disc rotated and the high-speed braiding machine operated at a braiding speed of 15 rpm, winding speed of 2 m/min, and braided pitch of 80 mm. Further, the fabricated CTBYs are wound around the bobbin and are braided again as aforementioned. The reciprocating movement from one disk to another is beneficial for the interconnection between the CTBYs in the formation of the BCFF. A continuous supply of yarn is provided by the rotation of the spool on the spindles, and the number of spindles required for winding the yarn depended on the number of feeding spindles. When the number of CTBY is 16, 24, 32, 40, 48, and 56, the fabricated BCFF is named BCFF-T16-C30, BCFF-T24-C30, BCFF-T32-C30, BCFF-T40-C30, BCFF-T48-C30, and BCFF-T56-C30, respectively. As for BCFF-T40, when the number of core yarn Tencel is 10, 20, 30, and 40, the fabricated evaporators are named BCFF-T40-C10, BCFF-T40-C20, BCFF-T40-C30, and BCFF-T40-C40, respectively. When the number the height of BCFF-T40-C30 is varied, the fabricated evaporators are named BCFF-Hs. When optimizing the parameters of the orthogonal test such as thickness, number, and height, only a single variable is regulated while the remaining parameters are kept constant.

Characterization: The morphology and microstructure of the samples are observed by a scanning electron microscope (FEI XL30, Sirion SEM). The water contact angle is tested by a wettability meter (KONO SL200KS). The surface temperature is recorded by an infrared camera (FLIR T620). The solar absorption is tested by UV-VIS-NIR Spectrophotometer (UV-

2550, Shimadzu) from 250 to 2500 nm equipped with an integrated sphere. Fourier transform infrared (FTIR) spectroscopy is conducted using a spectrometer (Nicolet iS50, Thermo Scientific). In the outdoor experiment, the water is taken from Dushu Lake and the Yellow Sea, China. The ion concentration is tracked by ICP Spectrometer (ICAP 6000 SERIES, Thermo Scientific).

Evaporation performance evaluation: A container filled with water is used to simulate the SSG process. The container is wrapped with polystyrene foam to concentrate heat. The experiment is conducted at room temperature about 25 °C and the humidity is about 50 %. The measurement point of solar intensity is located in the middle of the sample. The real-time mass loss is recorded by an electronic balance (Precisa, XB2200C). The simulated light source is provided by a solar simulator (Beijing CEAulight Technology, CEL-S500, AM 1.5G), and the solar intensity is calibrated with a light power meter (Beijing CEAulight Technology, CEL-NP2000).

The evaporation rate (ṁ) is calculated by the equation: [1]

$$\dot{m} = \frac{\Delta m}{St} \tag{1}$$

where Δm is the mass change of water during evaporation, S means the projected evaporation area, and t refers to the time of the evaporation process.

The corresponding energy efficiency (η) can be calculated by the following equation:[2]

$$\eta = \frac{\dot{m}\, E_v}{C_{opt} P_0} \tag{2}$$

where η is the evaporation efficiency, E_v means the vaporization enthalpy, C_{opt} refers to the optical concentration on the fabric, and P_0 denotes the solar irradiation power of 1 sun illumination.

The heat transfer (q) can be calculated using the following equations:[3-5]

$$q = q_{rad} + q_{conv} \tag{3}$$

$$q_{rad} = \varepsilon\sigma A_{rad} (T_M^4 - T_E^4) \tag{4}$$

$$q_{conv} = h A_{conv} (T_M - T_E) \tag{5}$$

Where q_{rad} is the radiative heat loss, and q_{conv} means the convective heat loss. A_{rad} and A_{conv} are the corresponding evaporation area, ε refers to the emissivity of the evaporator (i.e., 0.99), h is the convection heat transfer coefficient (5 $W \cdot m^{-2} \cdot K^{-1}$), σ denotes the Stefan-Boltzmann constant (i.e., 5.67×10^{-8} $W \cdot m^{-2} \cdot K^{-4}$), T_M and T_E are the temperature of the evaporation surface and the environment, respectively.

The numerical simulation of salt concentration distribution during the desalination process. Numerical simulation was conducted by COMSOL Multiphysics 5.5. The salinity gradually increases because of water content loss during desalination. The simulation was carried out according to the water content (w·m). The brine transport in the evaporator is expressed by: [6]

$$\nabla \cdot (\rho_w \mu_{wc} + \rho_w \mu_{wd}) = g_{evap} M_w \quad (6)$$

where μ_{wc} refers to the convection velocity ($\rho_w \nabla_{uw} \nabla_{wm}$) and μ_{wd} represents the diffusion velocity ($D_w \nabla_{wm}$, D_w denotes the effective diffusion coefficient). M_w is the molar mass of water. Among them, the μ_{wc} means equal to the brine transport velocity, and μ_{wd} is related to temperature, porosity, and water saturation. Therefore, the result of the salinity is w_s (w_s=1-w_w).

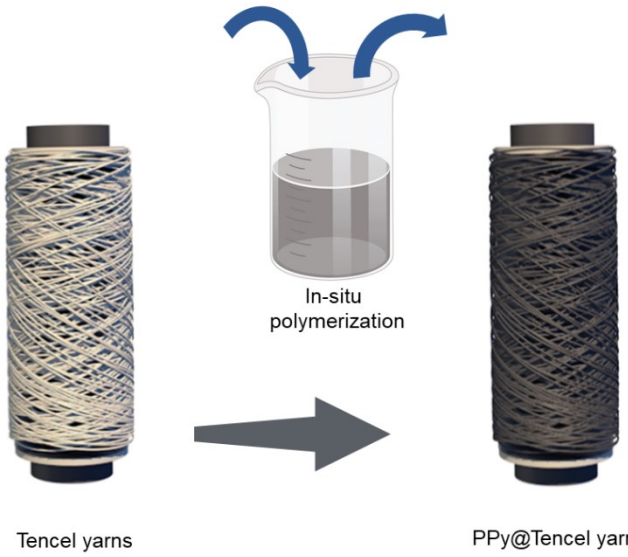

Fig. S1. The fabrication process of the in-situ polymerization of PPy on Tencels

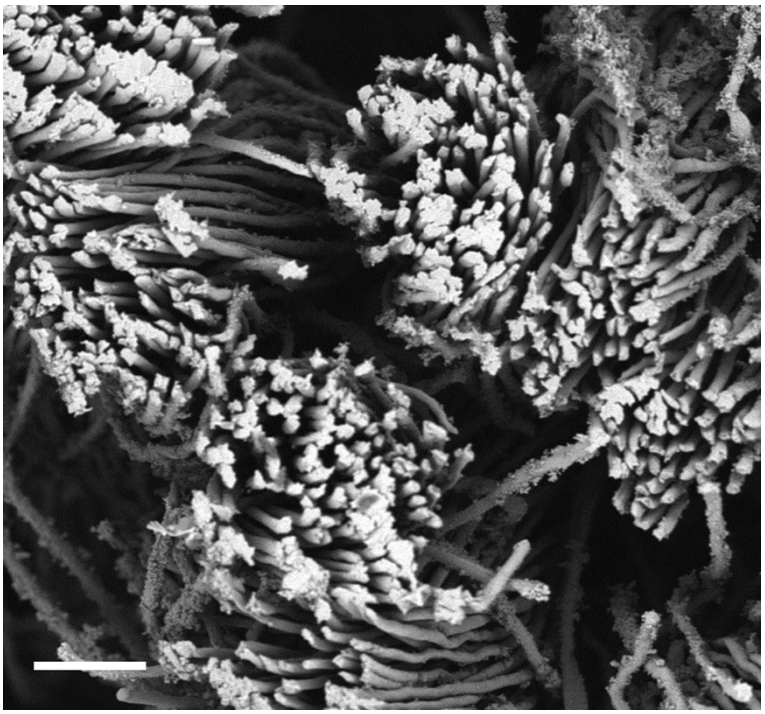

Fig. S2. SEM image of PPy@Tencel, (Scale bar: 100 μm).

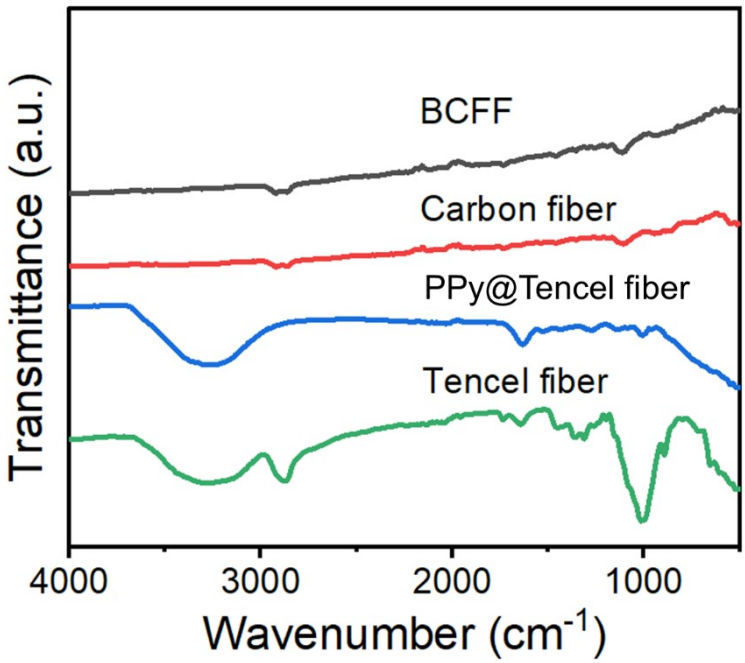

Fig. S3. FTIR spectra of carbon fiber, pristine Tencel, PPy@Tencel, and BCFF.

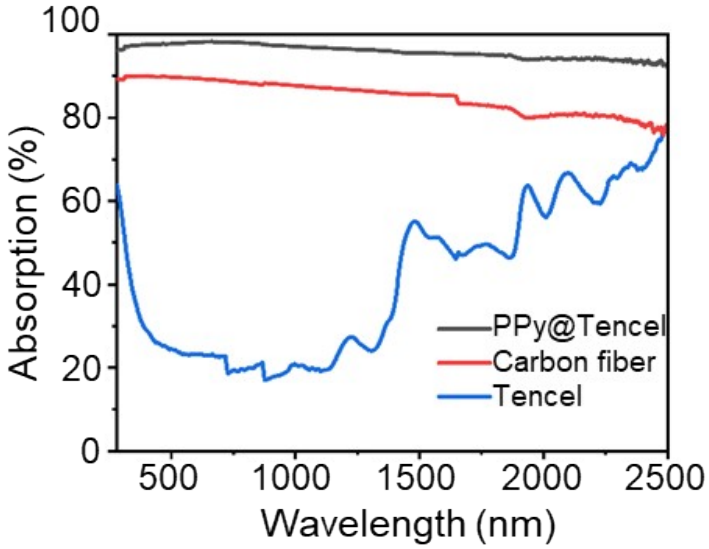

Fig. S4. Absorption spectra of carbon fiber, pristine Tencel, and PPy@Tencel in the 200−2500 nm wavelength range.

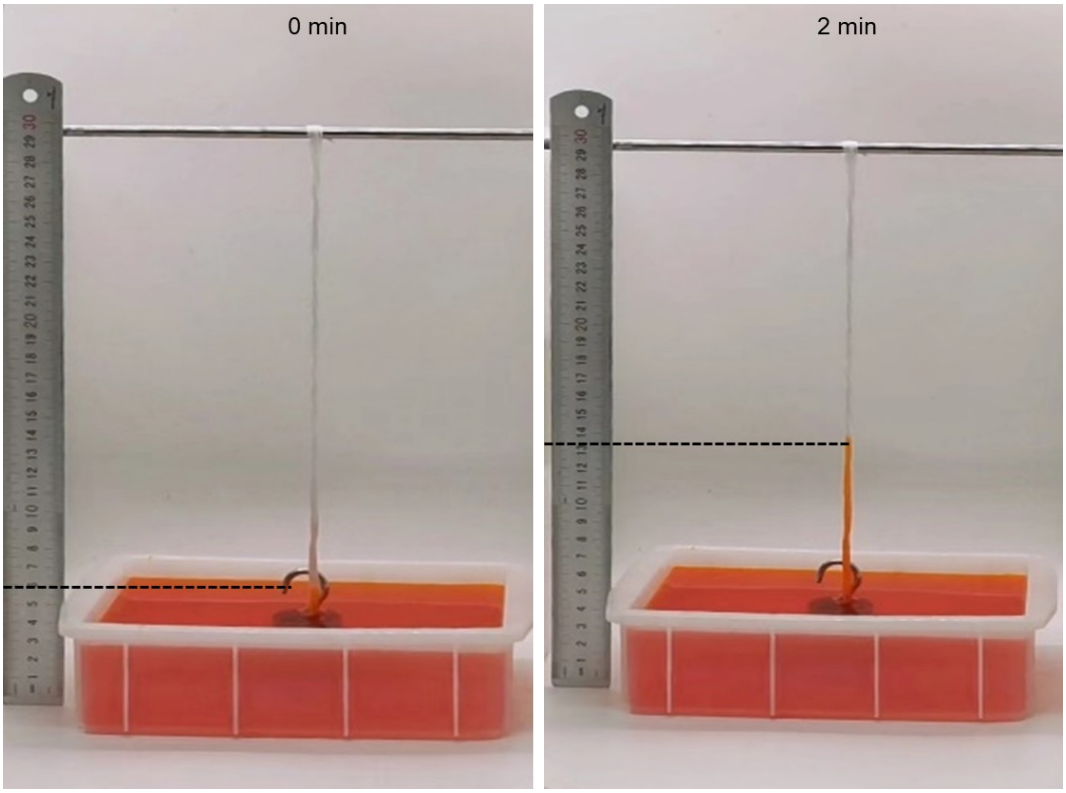

Fig. S5. The optical images show the water supply performance of Tencel fiber.

Fig. S6. The water content angle test of BCFF.

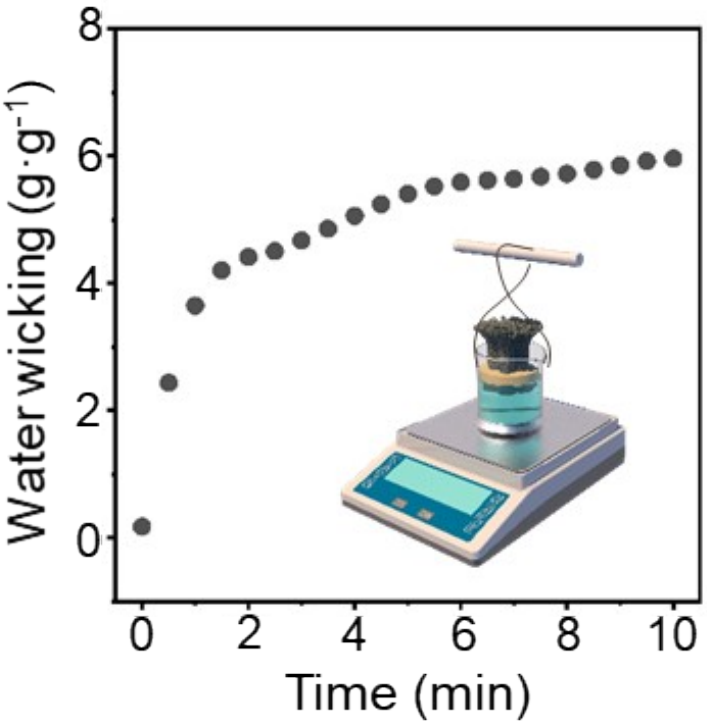

Fig. S7. The water-wicking rate of BCFF.

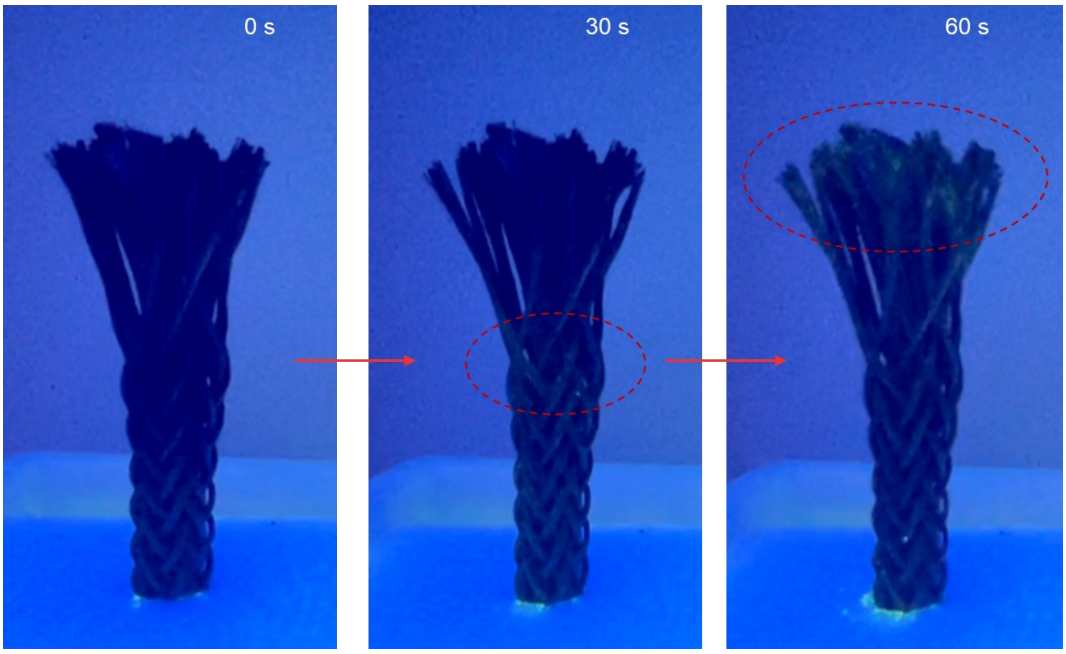

Fig. S8. The optical images show the water transport performance of BCFF with fluorescent dyes.

Fig. S9. The Optical images of the morphology of BCFF-Ts.

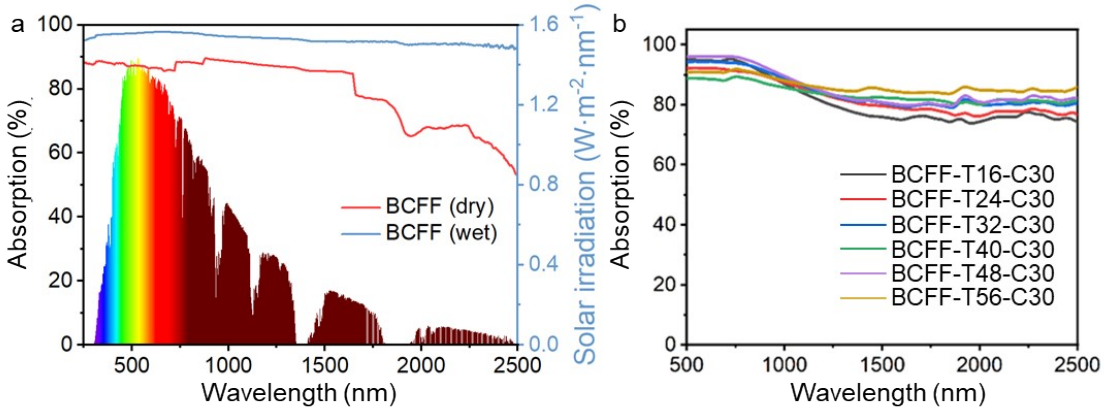

Fig. S10. (a) The absorption spectra of BCFF in the dry and wet state over the 200−2500 nm wavelength range. (b) Absorption spectra of BCFF-Ts over the 500−2500 nm wavelength range.

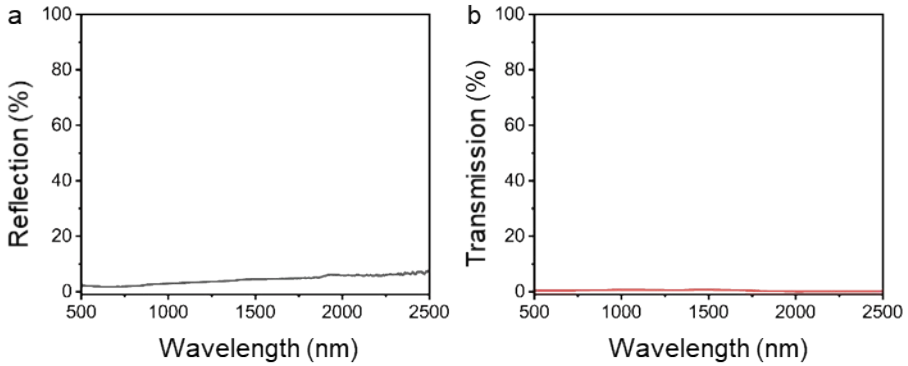

Fig. S11. (a) The reflection spectra and (b) transmission spectra of BCFF in the wet state over the 500−2500 nm wavelength range.

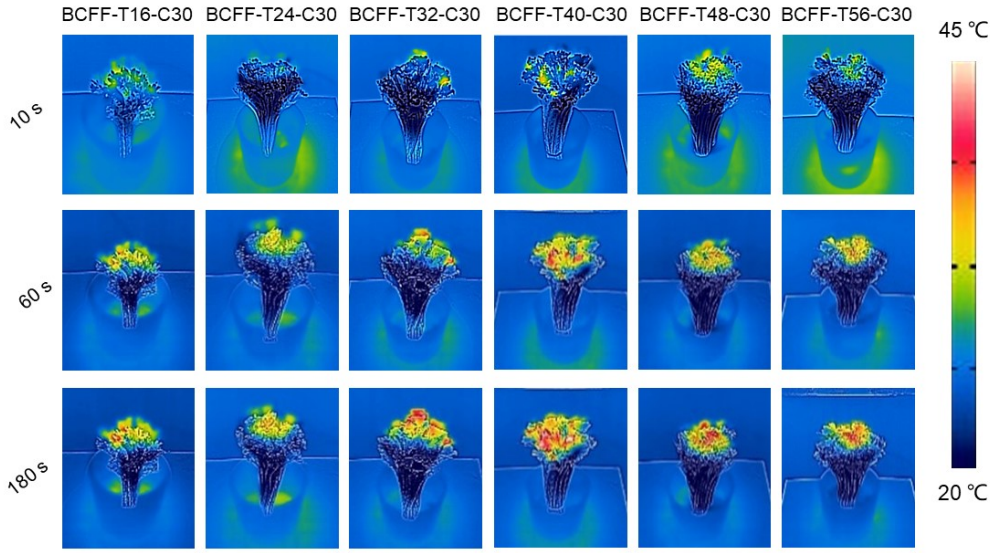

Fig. S12. Infrared images of BCFF-Ts evaporators under 1 sun illumination.

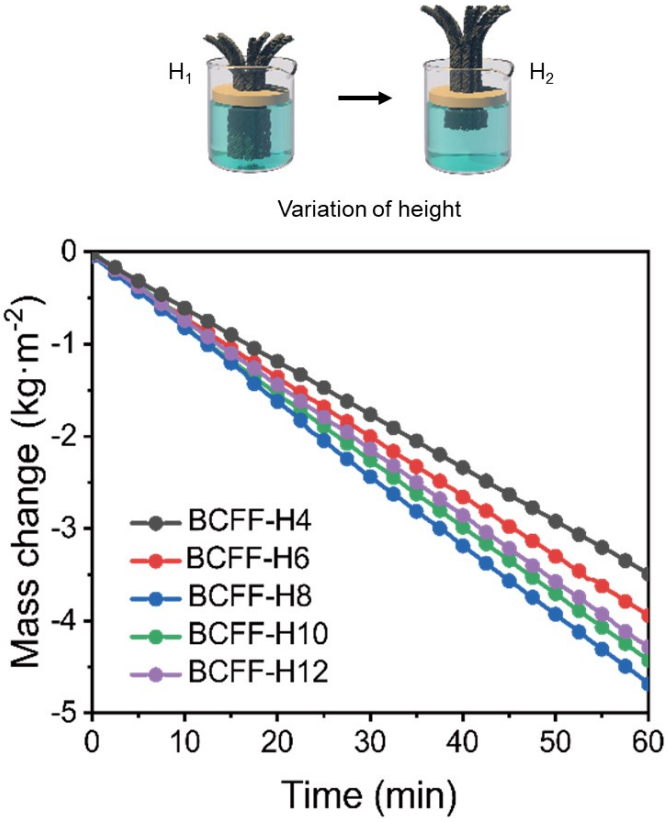

Fig. S13. The evaporation performance of BCFF-Hs under 1 sun illumination.

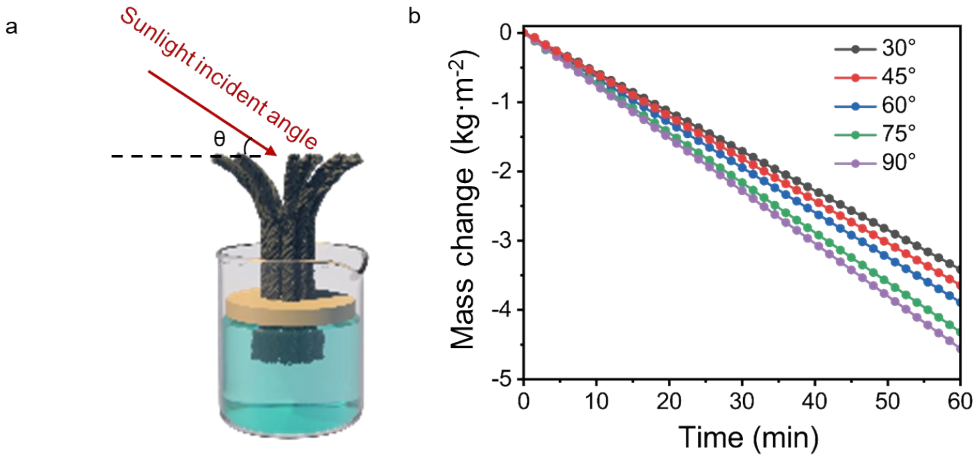

Fig. S14 (a) Schematic illustration of BCFF under solar illumination of varied incident angles. (b) The evaporation mass change of BCFF under 1 sun illumination of varied incident angles.

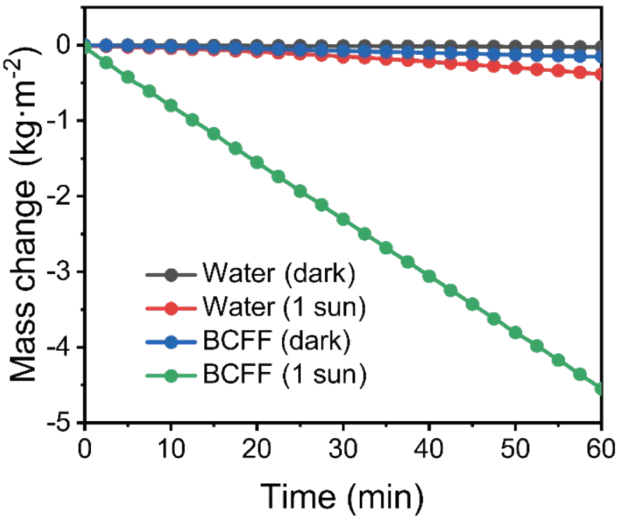

Fig. S15. Mass change of water caused by BCFF-T40-C30 and bulk water under 0 sun and 1 sun illumination.

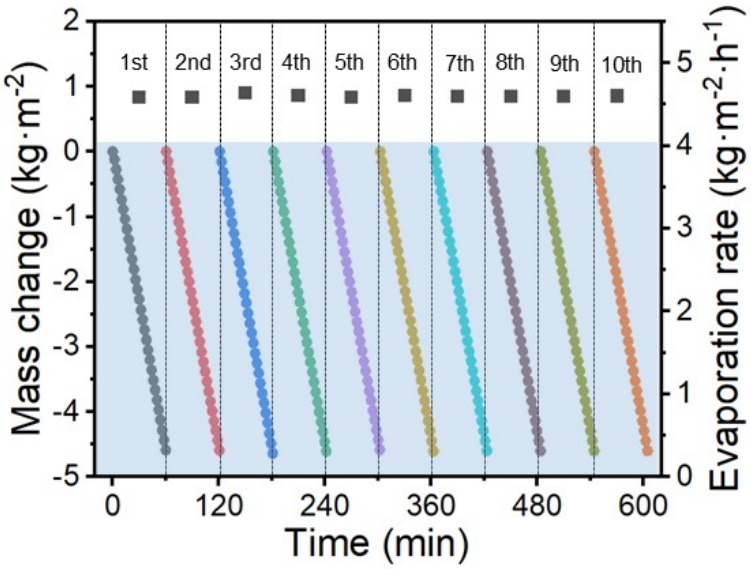

Fig. S16. The evaporation performance of BCFF-T40-C30 over 10 cycles (1 h per cycle).

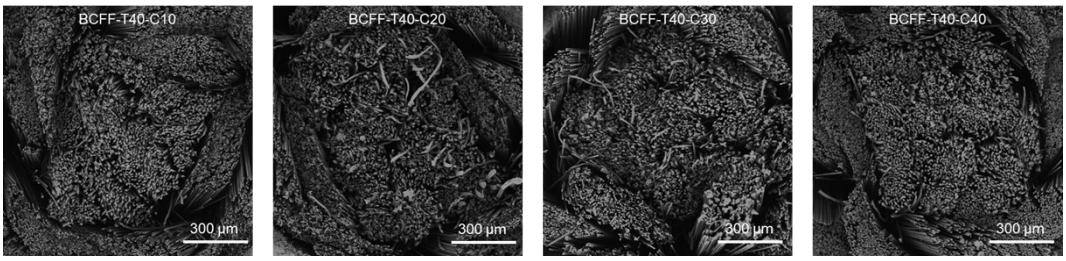

Fig. S17. SEM image of BCFF-T40-Cs, (Scale bar: 300 µm).

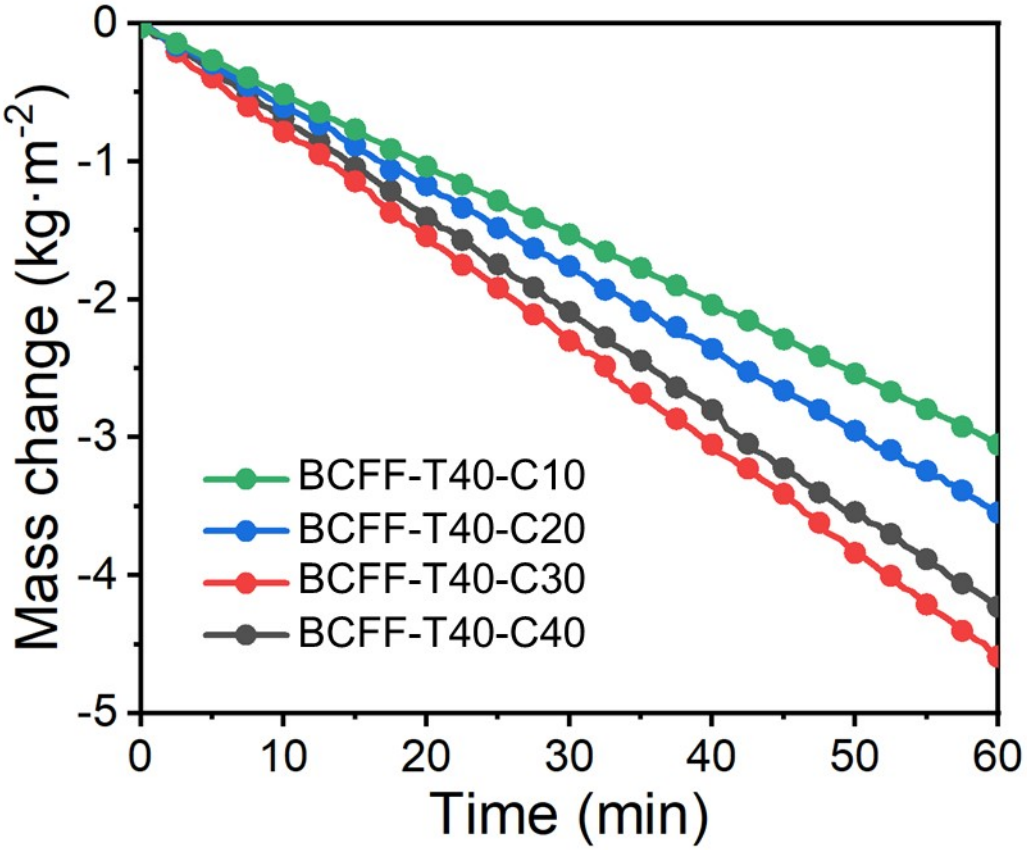

Fig. S18. The mass change of water caused by BCFF-T40-Cs under 1 sun illumination.

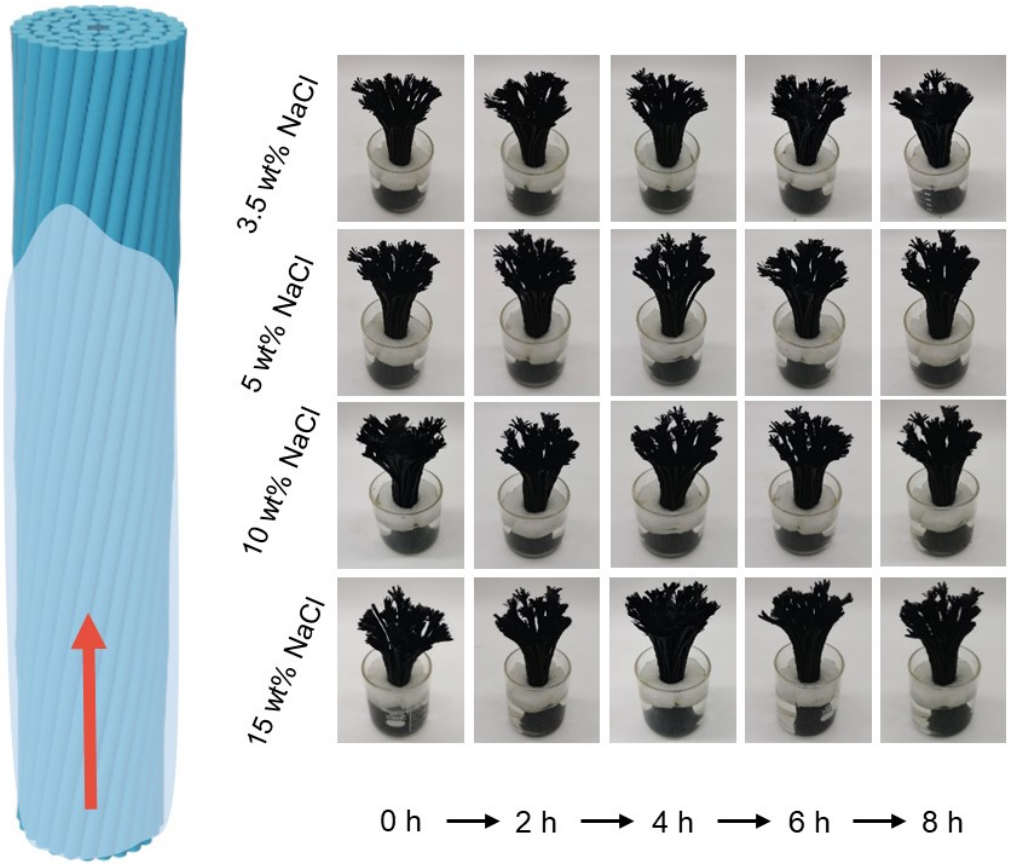

Fig. S19. Surface crystallization performance comparison of BCFF-T40-C30 in different brine concentrations after 8 h operation.

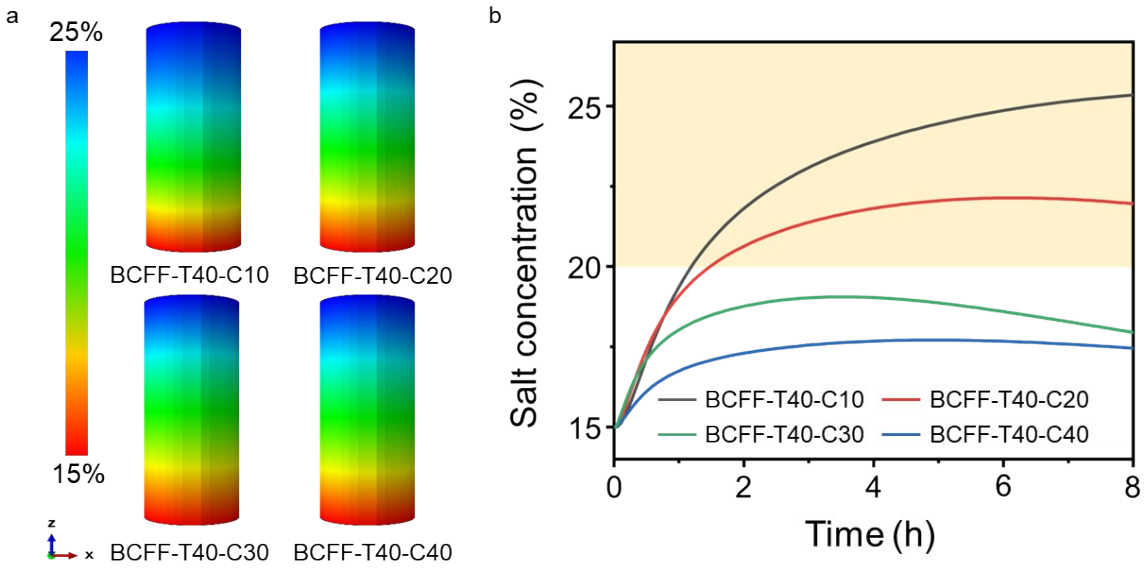

Fig. S20. COMSOL simulation of salt concentration changes during desalination in 15 wt% brine over 8 h operation.

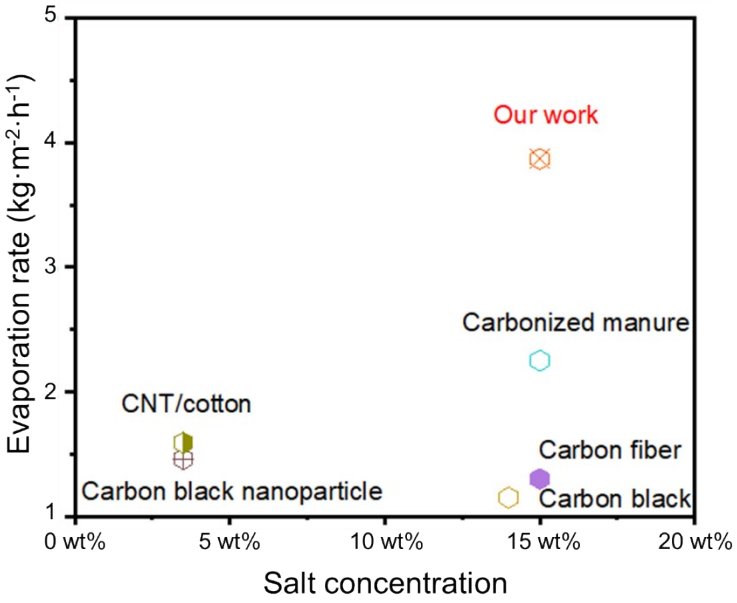

Fig. S21. Desalination rate comparison of recent works under 1 sun illumination. [7-11]

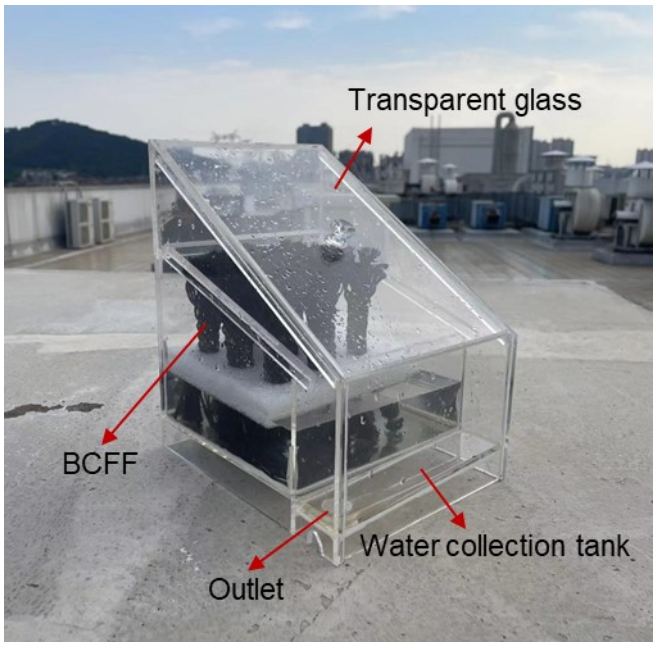

Fig. S22. Photograph of the outdoor desalination device in the open system.

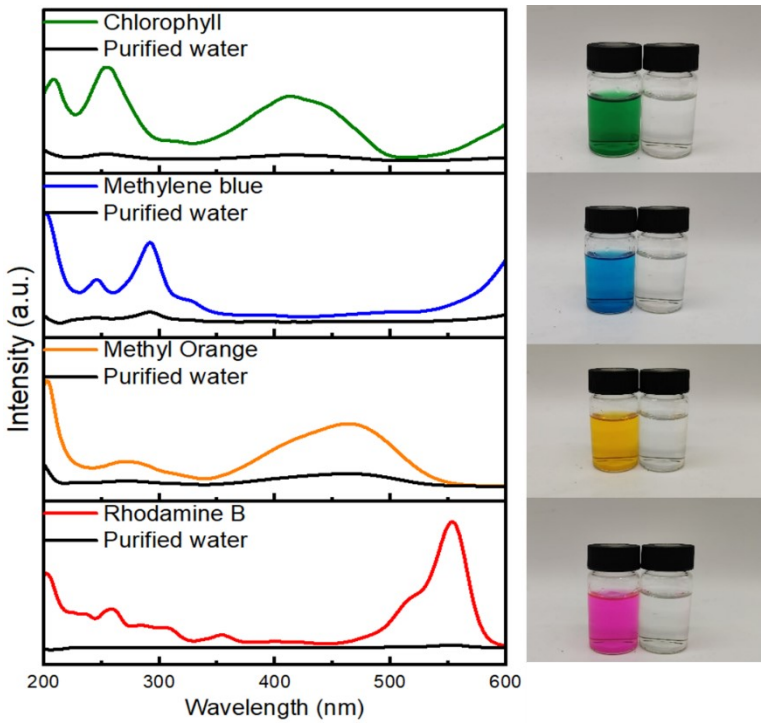

Fig. S23. UV−vis spectra of Congo red, rhodamine B, methylene blue, and methyl orange before and after purification.

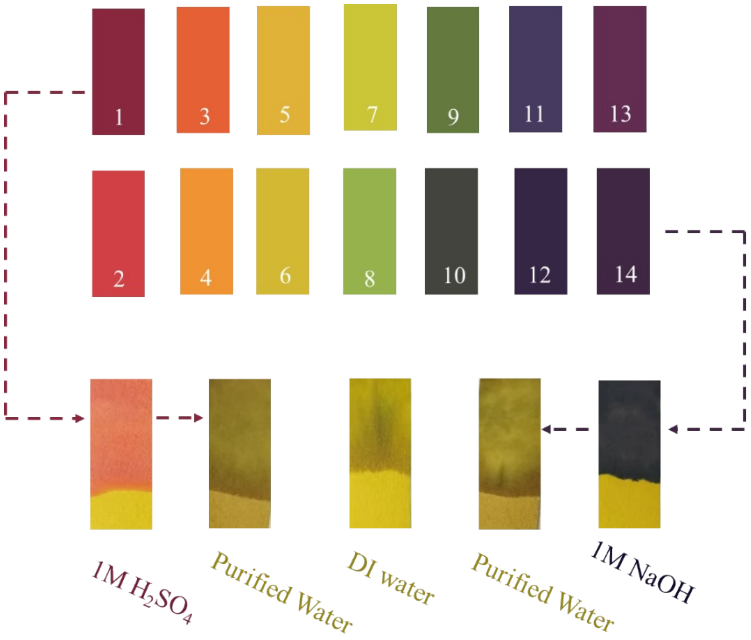

Fig. S24. PH values before and after the acidic and alkaline solutions are purified by BCFF.

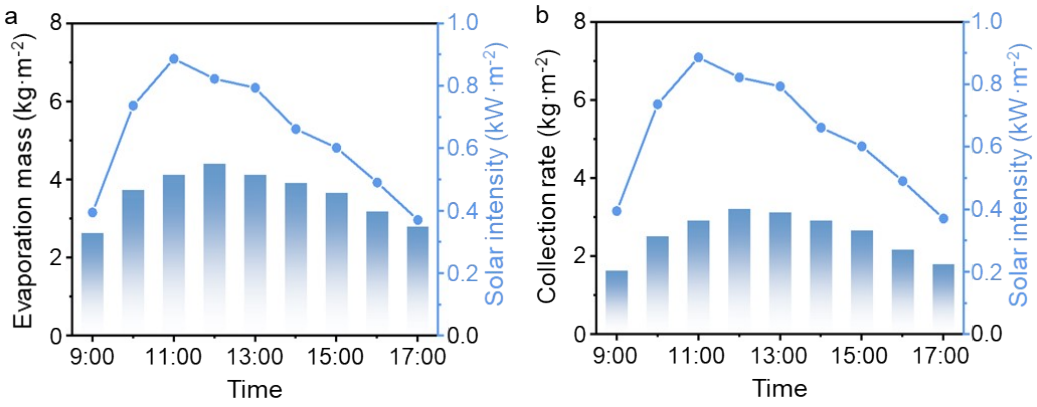

Fig. S25. (a) The evaporation mass of BCFF in the outdoor open system from 9 a.m. to 5 p.m. on October 5, 2022, in Wuhan, China. (b) The freshwater collection rate of BCFF in the outdoor closed system from 9 a.m. to 5 p.m. on October 5, 2022, in Wuhan, China.

Table S1 The detailed heat loss of BCFFs under 1 sun illumination.

Evaporator	Radiation loss (W)	Convection loss (W)	Total (W)
BCFF-T16-C30	0.0882	0.1349	0.2231
BCFF-T24-C30	0.1504	0.2277	0.3781
BCFF-T32-C30	0.2231	0.3346	0.5577
BCFF-T40-C30	0.3084	0.4553	0.7637
BCFF-T48-C30	0.2966	0.4424	0.7390
BCFF-T56-C30	0.2659	0.3996	0.6655

Reference

1. C. Ge, D. Xu, H. Du, Z. Chen, J. Chen, Z. Shen, W. Xu, Q. Zhang and J. Fang, *Adv. Fiber Mater.*, 2022, DOI: https://doi.org/10.1007/s42765-022-00228-6.
2. Z. Chen, Q. Li and X. Chen, *ACS Sustain. Chem. Eng.* , 2020, **8**, 13850-13858.
3. G. Cheng, X. Z. Wang, X. Liu, Y. R. He and B. V. Balakin, *Sol. Energy*, 2019, **194**, 415-430.
4. H. Li, Y. He, Y. Hu and X. Wang, *ACS Appl. Mater. Inter.*, 2018, **10**, 9362-9368.
5. J. Huang, Y. He, Y. Hu and X. Wang, *Sol. Energy Mater. Sol. Cells*, 2019, **203**.
6. Y. Chen, J. Yang, L. Zhu, S. Wang, X. Jia, Y. Li, D. Shao, L. Feng and H. Song, *Desalination*, 2023, **548**, 116287.
7. Y. Xiao, X. Wang, C. Li, H. Peng, T. Zhang and M. Ye, *J Environ. Chem. Eng.*, 2021, **9**, 105010.
8. Y. Tian, X. Liu, Z. Wang, A. Caratenuto, F. Chen, Y. Wan and Y. Zheng, *Desalination*, 2021, **520**, 115345.
9. X. Wang, Q. Gan, R. Chen, H. Peng, T. Zhang and M. Ye, *ACS Sustain. Chem. Eng.* , 2020, **8**, 7753-7761.
10. H. Kou, Z. Liu, B. Zhu, D. K. Macharia, S. Ahmed, B. Wu, M. Zhu, X. Liu and Z. Chen, *Desalination*, 2019, **462**, 29-38.
11. W. Zhao, H. Gong, Y. Song, B. Li, N. Xu, X. Min, G. Liu, B. Zhu, L. Zhou, X.-X. Zhang and J. Zhu, *Adv. Funct. Mater.*, 2021, **31**, 2100025.